

DETECTION OF THERMAL EMISSION FROM AN EXTRASOLAR PLANET

DAVID CHARBONNEAU,¹ LORI E. ALLEN,¹ S. THOMAS MEGEATH,¹ GUILLERMO TORRES,¹ ROI ALONSO,²
TIMOTHY M. BROWN,³ RONALD L. GILLILAND,⁴ DAVID W. LATHAM,¹ GEORGI MANDUSHEV,⁵
FRANCIS T. O'DONOVAN,⁶ AND ALESSANDRO SOZZETTI^{1,7}

Received 2005 February 3; accepted 2005 March 1

ABSTRACT

We present *Spitzer Space Telescope* infrared photometric time series of the transiting extrasolar planet system TrES-1. The data span a predicted time of secondary eclipse, corresponding to the passage of the planet behind the star. In both bands of our observations, we detect a flux decrement with a timing, amplitude, and duration as predicted by published parameters of the system. This signal represents the first direct detection of (i.e., the observation of photons emitted by) a planet orbiting another star. The observed eclipse depths (in units of relative flux) are 0.00066 ± 0.00013 at $4.5 \mu\text{m}$ and 0.00225 ± 0.00036 at $8.0 \mu\text{m}$. These estimates provide the first observational constraints on models of the thermal emission of hot Jupiters. Assuming that the planet emits as a blackbody, we estimate an effective temperature of $T_p = 1060 \pm 50$ K. Under the additional assumptions that the planet is in thermal equilibrium with the radiation from the star and emits isotropically, we find a Bond albedo of $A = 0.31 \pm 0.14$. This would imply that the planet absorbs the majority of stellar radiation incident upon it, a conclusion of significant impact to atmospheric models of these objects. We also compare our data to a previously published model of the planetary thermal emission, which predicts prominent spectral features in our observational bands due to water and carbon monoxide. This model adequately reproduces the observed planet-to-star flux ratio at $8.0 \mu\text{m}$; however, it significantly overpredicts the ratio at $4.5 \mu\text{m}$. We also present an estimate of the timing of the secondary eclipse, which we use to place a strong constraint on the expression $e \cos \omega$, where e is the orbital eccentricity and ω is the longitude of periastron. The resulting upper limit on e is sufficiently small that we conclude that tidal dissipation is unlikely to provide a significant source of energy interior to the planet.

Subject headings: binaries: eclipsing — infrared: stars — planetary systems — stars: individual (TrES-1) — techniques: photometric

1. INTRODUCTION

Extrasolar planets that transit their parent stars are particularly valuable, since they afford direct estimates of key physical parameters of the object. Moreover, it is only for bright stars that direct follow-up studies of the planet are likely to succeed. Indeed, the numerous follow-up observations of the brightest known transiting system HD 209458 (Charbonneau et al. 2000; Henry et al. 2000) include the detection (Charbonneau et al. 2002) and upper limits (Richardson et al. 2003a, 2003b; Deming et al. 2005) of absorption features in the planetary atmosphere, the discovery of a cloud of escaping hydrogen atoms (Vidal-Madjar et al. 2003), and a search for circumplanetary rings and Earth-sized satellites (Brown et al. 2001). The Optical Gravitational Lensing Experiment (OGLE) survey (Udalski et al. 2002a, 2002b, 2003, 2004) has yielded five transiting planets (Bouchy et al. 2004; Konacki et al. 2003, 2005; Moutou et al. 2004; Pont et al. 2004) with reasonably precise estimates of the planetary masses and radii; however, the direct follow-up studies described above are impeded for these objects because of their great distance and resulting faintness. The exclusive opportunities afforded by bright

systems have provided strong motivation for numerous wide-field, small-aperture surveys for these objects (Alonso et al. 2004; Bakos et al. 2004; Christian et al. 2004; Dunham et al. 2004; O'Donovan et al. 2004; Pepper et al. 2004). The first success for the wide-field approach occurred only recently with the detection of TrES-1 (Alonso et al. 2004). This hot Jupiter has a mass $M_p = (0.76 \pm 0.05)M_{\text{Jup}}$ and radius $R_p = (1.04^{+0.08}_{-0.05})R_{\text{Jup}}$ and is located 0.0394 AU from the central K0 V star (Sozzetti et al. 2004).

Soon after the discovery of TrES-1, we proposed for Director's Discretionary time on the *Spitzer Space Telescope* to monitor photometrically the TrES-1 system with the goal of detecting the thermal emission of the planet through observation of the secondary eclipse (i.e., the passage of the planet behind the star). Detection of this signal is of interest for several reasons. First, it would constitute the first direct detection of an extrasolar planet, i.e., the detection of photons emitted by the planet. Second, the amplitude of the secondary eclipse can be compared directly to theoretical models of the planetary atmosphere and, under the assumption of blackbody emission, yields an estimate of the effective temperature of the planet. Third, the timing and duration of the secondary eclipse place constraints on the orbital eccentricity that are much more restrictive than those from the radial velocity orbit alone. A nonzero eccentricity requires a source of excitation (such as a second planet), and the damping of this orbital eccentricity provides an internal energy source that could slow the contraction of the radius of the transiting planet (Bodenheimer et al. 2001, 2003). Conversely, a zero eccentricity would rule out this scenario.

In this paper, we present the detection of the thermal emission from the extrasolar planet TrES-1 and discuss the implications for our understanding of the planet.

¹ Harvard-Smithsonian Center for Astrophysics, 60 Garden Street, Cambridge, MA 02138; dcharbonneau@cfa.harvard.edu.

² Instituto de Astrofísica de Canarias, 38200 La Laguna, Tenerife, Spain.

³ High Altitude Observatory, National Center for Atmospheric Research, 3450 Mitchell Lane, Boulder, CO 80307.

⁴ Space Telescope Science Institute, 3700 San Martin Drive, Baltimore, MD 21218.

⁵ Lowell Observatory, 1400 West Mars Hill Road, Flagstaff, AZ 86001.

⁶ California Institute of Technology, 1200 East California Boulevard, Pasadena, CA 91125.

⁷ Home institution: Department of Physics and Astronomy, University of Pittsburgh, 100 Allen Hall, 3941 O'Hara Street, Pittsburgh, PA 15260.

2. OBSERVATIONS AND TIME SERIES PRODUCTION

The Infrared Array Camera (IRAC; Fazio et al. 2004) on *Spitzer* obtains simultaneous images in four bandpasses. A 5.2×5.2 field of view (FOV) is imaged in one pair of bandpasses (3.6 and 5.8 μm), and a nearly adjacent 5.2×5.2 FOV is imaged in the second pair (4.5 and 8.0 μm). The two blue channels employ InSb detectors, whereas the red channels use Si:As IBC detectors. All four arrays are 256×256 pixels.

We elected to monitor TrES-1 in only one channel pair (4.5 and 8.0 μm) to avoid repointing the telescope during the course of the observations. We chose not to dither the pointing in order to minimize the motion of the stars on the pixel array. We carefully selected the pointing position so that TrES-1 (2MASS J19040985+3637574: $J = 10.294$, $J - K = 0.475$) and two bright calibrators (2MASS J19041058+3638409: $J = 9.821$, $J - K = 0.557$; 2MASS J19040934+3639195: $J = 11.213$, $J - K = 0.703$) would avoid areas of the array with known bad pixels or significant gradients in the flat field as well as areas known to be affected by scattered starlight. We also ensured that a nearby star (2MASS J19040089+3639564: $J = 5.57$, $J - K = 0.941$) that was much brighter than the target would not fall into one of several regions outside the FOV that are known to result in significant scattered light on the detectors.

We observed the field for 5.6 hr spanning UT 2004 October 30–31. We obtained 1518 full-array images in each of the two bandpasses; the cadence was 13.2 s with an effective integration time of 10.4 s. The images were bundled in sets of 200, corresponding to the maximum number of images in a single Astronomical Observing Request (AOR). As the starting point in the following analysis, we used the IRAC Basic Calibrated Data (BCD) frames. These frames are produced by the standard IRAC calibration pipeline and include corrections for dark current, flat-fielding, detector nonlinearity, and conversion to flux units. We converted the time stamps in the image headers to Julian dates and adjusted these to correspond to the center of the integration. We then corrected these dates for the light travel time across the solar system, including the correction for the spatial separation of *Spitzer* and the Earth (an adjustment of approximately +29.7 s).

We evaluated the arithmetic centroid of the target and both calibrators in each image. We found that the pointing jitter was less than 0.05 pixels ($0''.06$) over the course of a single AOR, but offsets as large as 0.2 pixels ($0''.24$) occurred between AORs. These offsets were likely due to the reacquisition sequence that occurred automatically at the start of each AOR. Since these subpixel offsets introduce apparent variations in the recorded flux (clearly evident in our 4.5 μm photometry, as described below), deactivating this process would enable even greater photometric precision in future applications requiring multiple AORs.

We then performed aperture photometry on the images, using an aperture radius of 4.0 pixels and a sky estimate derived from an annulus of 15–25 pixels. (Note that we retained the use of relative fluxes, as opposed to magnitudes, throughout the analysis.) The aperture radius was selected to minimize the rms residual of the resulting time series for the calibrators. Apertures smaller than 3.5 pixels showed large deviations due to flux spilling out of the aperture, whereas radii larger than 4.5 pixels resulted in significantly degraded rms residuals due to increased sky background (particularly for the 8.0 μm channel, for which the sky is brighter). We also rejected the data from the first of the eight AORs, since these data showed increased noise that pre-

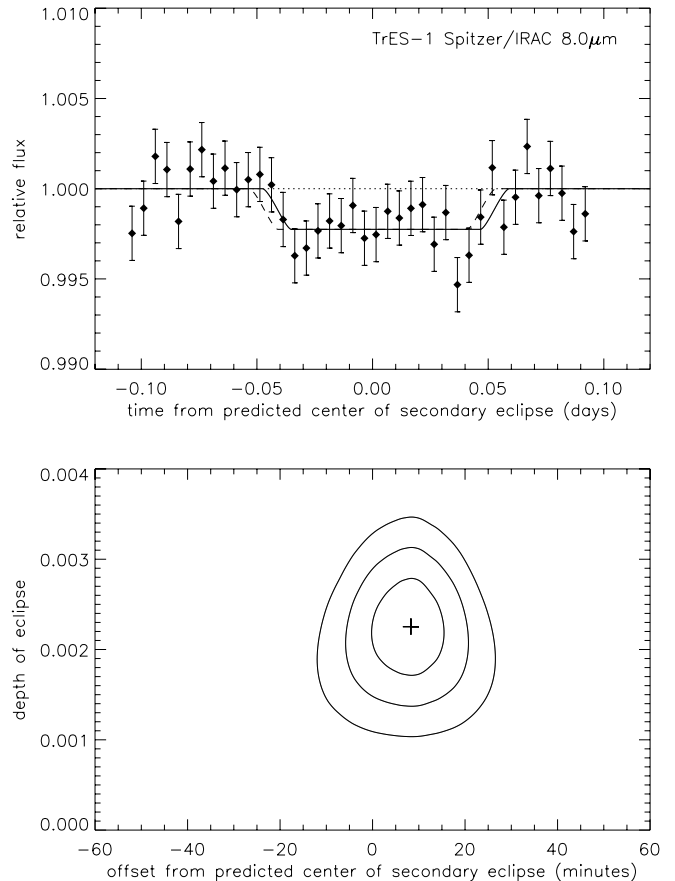


FIG. 1.—*Top*: Binned 8.0 μm time series. The best-fit model eclipse curve has a depth of $\Delta F_{\text{II}} = 0.00225$ and a timing offset of $\Delta t_{\text{II}} = +8.3$ minutes and is plotted as the solid line. A model of the same depth but $\Delta t_{\text{II}} = 0$ is shown as the dashed line. *Bottom*: The 1, 2, and 3 σ confidence ellipses on the eclipse depth and timing offset.

sumably resulted from the instrument reaching a new equilibrium at the settings specific to this campaign. (We performed aperture photometry on several dozen fainter stars in the FOV. Since many of the resulting time series showed a similar effect, we concluded that the omission of these data was justified.) We had planned for this possibility by centering the predicted time of secondary eclipse within the span of the last seven AORs. As a result, the first AOR occurred well outside the predicted duration of the secondary eclipse, and the omission of these data did not impact our conclusions. We also rejected very large single-point deviants (presumably radiation events), which removed a further 2.3% of the time series data.

The 8.0 μm time series for all three stars show an increasing trend in brightness over the duration of the observations, with a rise of roughly 1.5% from start to finish. We fitted a third-order polynomial to each of the two calibrators, calculated the average of these fits, and divided the target time series by this average. We then normalized the time series by evaluating the average of those time series data far from the predicted time of eclipse. The rms residual of the resulting normalized time series (as evaluated outside times of secondary eclipse) was 0.0085. We then binned the data into 40 bins so that each bin spanned 7.0 minutes and typically contained 32 individual measurements. The resulting binned time series is shown in Figure 1. The assigned error bars in that figure are the rms residual of the unbinned data divided by the square root of the number of data points in that bin.

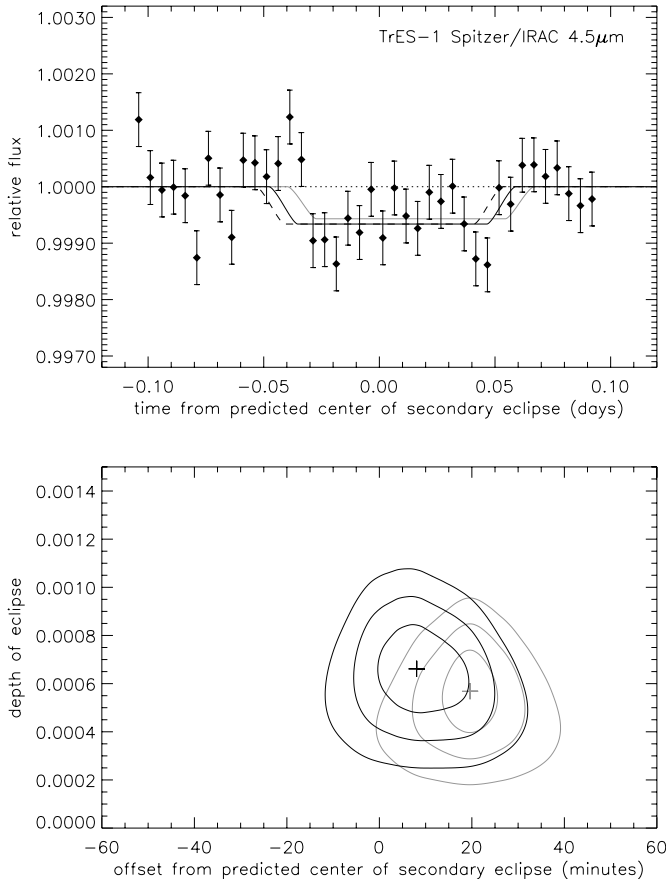


FIG. 2.—*Top*: Binned $4.5 \mu\text{m}$ time series. The best-fit model eclipse curve [excluding the data at times $-0.05 < t \text{ (days)} < -0.03$; see text] has a depth of $\Delta F_{\text{II}} = 0.00066$ and a timing offset of $\Delta t_{\text{II}} = +8.1$ minutes and is plotted as the solid black line. A model of the same depth but $\Delta t_{\text{II}} = 0$ is shown as the dashed line. The best-fit model when these additional 9.8% of data are included is shown as the gray line; the estimated depth is similar, but a significant timing offset is found. *Bottom*: The black ellipses are the 1, 2, and 3 σ confidence ellipses on the eclipse depth and timing offset for the restricted data set; the corresponding ellipses for the complete data set are shown in gray.

The $4.5 \mu\text{m}$ data showed no overall brightness trend, in contrast to what was seen for the $8.0 \mu\text{m}$ data. These data did, however, show photometric variations with a typical amplitude of 0.5% that clearly correlated with centroid position. There are several possible explanations for this effect: (1) the flat field (which is constructed from images of the sky over regions of high zodiacal light emission) is less precise at these shorter wavelengths, since the zodiacal emission is less; (2) the $4.5 \mu\text{m}$ InSb array may possess intrapixel sensitivity variations, and this effect is more acute at these shorter wavelengths because of the greater degree of undersampling; (3) the $4.5 \mu\text{m}$ observations are exposed to greater relative well depth and may enter the regime in which the pipeline linearity correction may not be adequate, resulting in apparent photometric variations that correlate with concentration of light in the central brightest pixel. We modeled each of these scenarios in detail and found that each (or a combination of several) could plausibly explain the photometric variations. The final approach we adopted was simply to decorrelate the photometric time series of the target versus X and Y positions and then quantify any potential attenuation in the signal through the modeling procedure described in § 3. As an additional test, we applied this decorrelation procedure to one of the two other bright stars in the FOV (the other

available calibrator was nearing saturation in these images), and it resulted in a time series that showed no significant deviations from a constant brightness. After decorrelation, the rms residual of the normalized time series for the target star was 0.0027, a factor of 3.1 smaller than the $8.0 \mu\text{m}$ data (owing to the greater number of photons recorded at these shorter wavelengths). We then binned the time series and assigned error bars in the same fashion as the $8.0 \mu\text{m}$ data. The final binned time series is shown in Figure 2.

3. ANALYSIS OF TIME SERIES

In order to evaluate the statistical significance of the signal, and to estimate its amplitude and timing, we created a model eclipse curve by assuming the system parameters as derived by Sozzetti et al. (2004): $R_* = 0.83 R_{\odot}$, $R_p = 1.04 R_{\text{Jup}}$, $i = 89.5^\circ$, and $a = 0.0394 \text{ AU}$. We calculated the predicted time of center of secondary eclipse to be $t_{\text{II}}^{\text{predicted}} = 2453309.52363 \pm 0.00052 \text{ HJD}$, based on the period and time of center of transit published by Alonso et al. (2004) and the assumption of a circular orbit ($e = 0$). The uncertainty in this prediction is much less than that of our estimate of the observed time of secondary eclipse (below) and hence is not a significant source of error. We likewise neglected the apparent delay in the time of secondary eclipse (relative to the times of primary eclipse) resulting from the light-travel time across the TrES-1 system, $2a/c = 39.3 \text{ s}$. We scaled the model eclipse depth to an amplitude ΔF_{II} , shifted it by a time Δt_{II} , and evaluated the χ^2 of the resulting fit to the unbinned time series. We repeated this procedure over a grid of assumed values for ΔF_{II} and Δt_{II} . Throughout this modeling procedure we analyzed the unbinned time series (binned data are shown in Figs. 1 and 2 for clarity).

For the $8.0 \mu\text{m}$ time series, the estimated eclipse depth was $\Delta F_{\text{II}} = 0.00225 \pm 0.00036$, and the timing offset was $\Delta t_{\text{II}} = +8.3 \pm 5.2$ minutes. The minimum of the χ^2 was $\chi^2 = 1238.2$ for $(N - 2) = 1280$ degrees of freedom (dof). The reduced χ^2 was therefore $\chi^2/(N - 2) = 0.97$, indicating an excellent fit to the data. In Figure 1, we show the binned data overplotted with the best-fit model and a contour plot showing the corresponding limits on ΔF_{II} and Δt_{II} .

For the $4.5 \mu\text{m}$ time series, the same procedure initially yielded an eclipse depth of $\Delta F_{\text{II}} = 0.00057 \pm 0.00013$ and a timing offset of $\Delta t_{\text{II}} = +19.6 \pm 6.6$ minutes. Formally, this offset in the time of secondary eclipse is statistically very significant. However, we noted that a small subset (9.8%) of the data near the time of ingress (spanning dates $-0.05 < t - t_{\text{II}}^{\text{predicted}} < -0.03$) was entirely responsible for the displacement in the best-fit value of Δt_{II} . Upon closer scrutiny, we found these data to be suspicious for two reasons. First, they originated from the AOR representing the largest displacement in centroid position and hence may not be well corrected by our decorrelation method. Second, if these data are valid, the implied duration of the secondary eclipse is too short to be physically plausible (since the egress occurred at the predicted time). As a test, we repeated the fitting procedure but gave these suspect data zero statistical weight. The resulting eclipse depth was $\Delta F_{\text{II}} = 0.00066 \pm 0.00013$, consistent with the previous value. However, the timing offset was reduced to $\Delta t_{\text{II}} = +8.1 \pm 6.6$ minutes. Since we are uncertain whether this discrepancy is in fact instrumental in nature, we simply treat the difference in the two estimates of Δt_{II} as indicative of the possible level of systematic error in the $4.5 \mu\text{m}$ eclipse time. The minimum of the χ^2 was $\chi^2 = 1220.9$ for $(N - 2) = 1153$ dof. The reduced χ^2 was therefore $\chi^2/(N - 2) = 1.06$, indicating a good fit to the data. In Figure 2, we show the

binned data overplotted with both model fits and a contour plot showing the corresponding limits on ΔF_{II} and Δt_{II} resulting from each analysis.

Of further concern is that the decorrelation procedure might attenuate the signal in the 4.5 μm time series. In order to quantify this effect, we injected eclipses in the raw time series with depths of $\Delta F_{\text{II}} = \{0.0005, 0.0010\}$. We then subjected these modified time series to the same procedures of decorrelation and χ^2 fitting. The derived best-fit eclipse depths were $\Delta F_{\text{II}} = \{0.00110 \pm 0.00013, 0.00155 \pm 0.00013\}$ (respectively), indicating that virtually no attenuation had occurred (i.e., the derived signal depths were found to be the sum of the original signal and the injected signal).

In summary, we find eclipse depths of $\Delta F_{\text{II}} = 0.00225 \pm 0.00036$ (8.0 μm) and $\Delta F_{\text{II}} = 0.00066 \pm 0.00013$ (4.5 μm). Our best estimate of the time of secondary eclipse is $t_{\text{II}} = 2453309.5294 \pm 0.0036$ HJD, corresponding to a timing offset of $\Delta t_{\text{II}} = +8.3 \pm 5.2$ minutes from the prediction based on a circular orbit and the period and time of transit published in Alonso et al. (2004). Because of the large systematic uncertainty in the timing estimate based on the 4.5 μm data, the derived value of Δt_{II} is essentially dictated by the 8.0 μm data.

4. DISCUSSION AND CONCLUSIONS

4.1. Planetary Emission

If we denote the planetary and stellar surface fluxes by $F_p(\lambda)$ and $F_*(\lambda)$, respectively, then the predicted signal in a given bandpass is prescribed by

$$\Delta F_{\text{II}} \simeq \left(\frac{R_p}{R_*}\right)^2 \frac{\int F_p(\lambda) S(\lambda) (\lambda/hc) d\lambda}{\int F_*(\lambda) S(\lambda) (\lambda/hc) d\lambda}, \quad (1)$$

where $S(\lambda)$ is the appropriate IRAC spectral response function⁸ in units of [e^- /photon]. In this approach, we neglect the contribution from reflected starlight to the observed values of ΔF_{II} , which could be as large as $(R_p/a)^2 \simeq 0.00016$ (Charbonneau et al. 1999) for the TrES-1 system. The ratio $(R_p/R_*)^2$ in equation (1) is very accurately constrained by transit observations and hence contributes little uncertainty. In the following discussion, we assume a model for the stellar flux $F_*(\lambda)$ calculated⁹ by R. Kurucz (2005, private communication; Kurucz 1992, 1993) for the stellar parameters as derived in Sozzetti et al. (2004). We note that a Planck curve should not be assumed for the stellar flux in equation (1), since the stellar flux at infrared wavelengths is significantly less than the prediction from a blackbody of the stellar effective temperature.

Using equation (1), we can convert the eclipse depths ΔF_{II} into band-dependent brightness temperatures $T_{4.5 \mu\text{m}}$ and $T_{8.0 \mu\text{m}}$ by substituting $F_p(\lambda) = \pi B_\lambda(T)$, where $B_\lambda(T)$ denotes the Planck curve. Minimizing the value of $\chi^2(T)$ for each of the two bands, we estimate brightness temperatures of $T_{4.5 \mu\text{m}} = 1010 \pm 60$ K and $T_{8.0 \mu\text{m}} = 1230 \pm 110$ K. Based on the modest discrepancy between these estimates of the brightness temperature, we find that the planetary emission is somewhat inconsistent with that of a blackbody. For the purposes of discussion, we initially consider the scenario in which the planet is assumed to emit as a blackbody; we then reevaluate our results

in the light of a more sophisticated model of the planetary emission.

Treating the planetary emission as a Planck curve of temperature T_p , we modify the procedure described in the previous paragraph, minimizing the summed value of $\chi^2(T_p)$ for the two measurements of ΔF_{II} . In this manner, we estimate the planetary temperature to be $T_p = 1060 \pm 50$ K. Under the further assumption that the planet is in thermal equilibrium with the stellar radiation, the planetary equilibrium temperature is prescribed by

$$T_{\text{eq}} = T_*(R_*/2a)^{1/2} [f(1-A)]^{1/4} \simeq 1163 [f(1-A)]^{1/4} \text{ K}, \quad (2)$$

where A is the wavelength-integrated Bond albedo (the fraction of energy reemitted relative to the amount received), and the factor f is 1 if the planetary emission is isotropic and 2 if only the day side of the planet reradiates the absorbed heat. We note that this approach neglects the contribution from the intrinsic luminosity of the planet, which results from ongoing contraction. Substituting our temperature estimate T_p for T_{eq} in equation (2), we find $[f(1-A)] \simeq 0.69 \pm 0.14$. If we further assume that the emission is isotropic ($f = 1$), this implies that the Bond albedo is $A \simeq 0.31 \pm 0.14$. The conclusion would be that the planet likely absorbs the majority of radiation incident upon it, a realization of significant impact to models of hot Jupiter atmospheres (see Baraffe et al. 2003, Barman et al. 2001, Burrows 2005, Burrows et al. 2001, Chabrier et al. 2004, Cho et al. 2003, Marley et al. 1999, Seager et al. 2000, Sudarsky et al. 2003, and references therein). A low albedo would also be consistent with the upper limits reported by searches for reflected light from other hot Jupiters (Charbonneau et al. 1999; Collier Cameron et al. 2002; Leigh et al. 2003), although we note that those studies constrained a combination of the wavelength-dependent geometric albedo and phase function, whereas the results presented here serve to constrain the wavelength-integrated and phase-integrated quantity A . We reiterate that this discussion assumes isotropic emission; if $f > 1$, then larger values of the Bond albedo A would be permitted.

As noted above, the assumption of blackbody emission is not supported by the discrepancy (albeit a modest one) in the brightness temperature estimates. In particular, the emission at 4.5 μm is less than and the emission at 8.0 μm is larger than that predicted for a blackbody of $T_p = 1060$ K. Numerous theoretical models of the emission spectra of hot Jupiters have been presented in the literature (see Burrows 2005 and references therein). Despite the variety of published models, the consensus is that large deviations from the Planck curve are predicted. In order to illustrate such deviations, we consider a model¹⁰ for the planetary flux presented by Sudarsky et al. (2003). We select the model for 51 Peg b, since, of the available choices, that planet most resembles TrES-1 in mass and degree of stellar insolation. We divide the model fluxes by those of the stellar model described above; the resulting prediction for the wavelength-dependent flux ratio is shown in Figure 3, overplotted with the two available data points. It should be noted that no parameters have been adjusted to improve the model fit, and, in particular, the model has not been renormalized. Although the model prediction is roughly consistent with the observed value at 8.0 μm , the model overpredicts the flux ratio at 4.5 μm . The emergent flux in the spectral region spanned by the IRAC bandpasses is

⁸ IRAC spectral response tables are available at http://ssc.spitzer.caltech.edu/irac/spectral_response.html.

⁹ The model for the stellar flux as calculated by R. Kurucz is available at <http://kurucz.harvard.edu/stars/KOIV/>.

¹⁰ This model is publicly available at <http://zenith.as.arizona.edu/~burrows/sbh/sbh.html>.

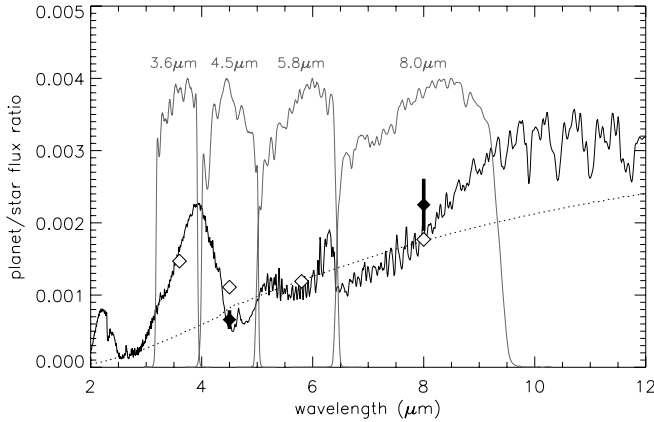


FIG. 3.—Solid black line shows the Sudarsky et al. (2003) model hot Jupiter spectrum divided by the stellar model spectrum (see text for details). The open diamonds show the predicted flux ratios for this model integrated over the four IRAC bandpasses (which are shown in gray and renormalized for clarity). The observed eclipse depths at 4.5 and 8.0 μm are overplotted as black diamonds. No parameters have been adjusted to the model to improve the fit. The dotted line shows the best-fit blackbody spectrum (corresponding to a temperature of 1060 K), divided by the model stellar spectrum. Although the Sudarsky et al. (2003) model prediction is roughly consistent with the observations at 8.0 μm , the model overpredicts the planetary flux at 4.5 μm . The prediction of a relatively large flux ratio at 3.6 μm should be readily testable with additional IRAC observations.

dominated by the presence of water and carbon monoxide; methane is not expected to be spectroscopically prominent, since CO is the preferred repository for carbon at these warm atmospheric temperatures. The predicted emission peak near 4 μm results from a window of low opacity that is constrained by significant water absorption bands blueward of the peak and absorption bands of both water and CO redward of it. An additional source of opacity in this region could suppress the flux to the low level that is observed; otherwise, it may be that the CO (1–0) fundamental band that overlaps the red half of the 4.5 μm bandpass is more prominent than the model predicts. Deming et al. (2005) have recently presented a stringent upper limit on the spectroscopic signature of CO for HD 209458b. That study utilized the technique of transmission spectroscopy (as opposed to emission) and examined a different band, the (2–0) transition at 2.3 μm . A detailed comparison of theoretical atmospheric models to both the results presented here and that earlier study would be fruitful.

We note that *Spitzer* observations of TrES-1 in the two additional IRAC bands (3.6 and 5.8 μm) would likely prove diagnostic of the planetary atmosphere. In particular, the model shown in Figure 3 predicts a large excess of emission in the 3.6 μm bandpass over the prediction of the best-fit blackbody spectrum. IRAC observations of HD 209458 would be facilitated by the greater apparent brightness of that system; however, detector saturation limits will require the use of a subarray mode, which may degrade the photometric stability. If in fact the IRAC subarray mode is as photometrically stable as the full-array mode, an additional scientific opportunity will be enabled. By gathering high-cadence photometric observations during times of ingress and egress of secondary eclipse, it may be possible to discern differences in the shape of the light curve from the prediction of a uniformly illuminated disk. Such observations would thus serve to resolve *spatially* the planetary emission across the dayside portion of the planetary disk. Moreover, the variations observed during ingress and egress will be complementary; toward the end of ingress, only the trailing edge of

the planet is unocculted, whereas during the initial portion of egress, only the leading edge of the planet is revealed. Detailed dynamical models of this planet’s atmosphere (Cho et al. 2003; Menou et al. 2003; Cooper & Showman 2005) predict significant atmospheric flows in response to the large incident stellar radiation on the day side. In particular, some models predict the presence of a hot spot, shifted downstream from the subsolar point because of the equatorial atmospheric flow. One effect of such a feature would be to shift the apparent center of the time of secondary eclipse. As a result, an apparent offset in the time of secondary eclipse from the prediction of a circular orbit may be induced even if the eccentricity is zero. Although such an offset is not detected for the TrES-1 system with high significance, we encourage theoretical calculations to evaluate whether apparent offsets of ~ 8 minutes (i.e., $\sim 1/4$ of the planetary disk crossing time) are plausible.

4.2. Orbital Eccentricity

The detection of the secondary eclipse is also of interest because it places constraints on the orbital eccentricity in addition to those provided by the radial velocity observations. A nonzero value of the orbital eccentricity could produce a measurable shift in the separation of the times of center of primary (t_I) and secondary (t_{II}) eclipse away from a half-period. The approximate formula for the offset (see Kallrath & Milone 1999, p. 60; Charbonneau 2003) is

$$\frac{\pi}{2P} \left(t_I - t_{II} - \frac{P}{2} \right) \simeq e \cos \omega, \quad (3)$$

where P is the orbital period and ω is the longitude of periastron; the expression in parentheses is precisely the offset Δt_{II} we have estimated earlier. Thus, we find that e and ω must satisfy

$$e \cos \omega \simeq \frac{\pi \Delta t_{II}}{2P} \simeq 0.0030 \pm 0.0019. \quad (4)$$

From this equation, a value of e may be estimated if an independent measure of ω exists. In particular, we note that an eccentric orbit also affects the relative durations of the primary (Θ_I) and secondary (Θ_{II}) eclipses according to

$$\frac{\Theta_I - \Theta_{II}}{\Theta_I + \Theta_{II}} \simeq e \sin \omega. \quad (5)$$

Thus, in principle, the separate dependencies of equations (3) and (5) on ω permits a direct evaluation of e . In practice, however, since the size of the second effect is proportional to only the duration of the eclipse (as opposed to the orbital period; eq. [3]), the relative uncertainty that results in estimates of the duration of the secondary eclipse is too great to be useful.

The most robust limits on e are obtained by using all available information on the geometry of the orbit, namely, the times of transit, the radial velocities, and the time of secondary eclipse reported here. Constraints on the eccentricity come mainly from the radial velocities and the time of secondary eclipse. The individual transit observations (listed in Table 1) are described by Alonso et al. (2004), with the exception of event number 12, which was observed at the IAC 80 cm telescope after that paper went to press. Of the 12 transit timings available, we excluded the one from the University of Colorado Sommers-Bausch Observatory (SBO), as it is discrepant by more than 6σ ; we also note that anomalies in the ingress and egress of that event are apparent in Figure 1 of Alonso et al. (2004). For the radial

TABLE 1
TIMES OF PRIMARY AND SECONDARY ECLIPSE

Event	Type	HJD	N_{eclipsed}	σ_{HJD}	$(O-C)^a$	$(O-C)/\sigma_{\text{HJD}}^a$	$(O-C)^b$	$(O-C)/\sigma_{\text{HJD}}^b$
1.....	Primary	2,452,847.4363	-112.0	0.0015	-0.0022	-1.45	-0.0023	-1.51
2.....	Primary	2,452,850.4709	-111.0	0.0016	+0.0023	+1.48	+0.0022	+1.42
3.....	Primary	2,452,856.5286	-109.0	0.0015	-0.0002	-0.12	-0.0003	-0.18
4.....	Primary	2,452,868.6503	-105.0	0.0022	+0.0013	+0.59	+0.0012	+0.55
5.....	Primary	2,453,171.6523	-5.0	0.0019	-0.0035	-1.81	-0.0035	-1.80
6.....	Primary	2,453,174.6864	-4.0	0.0004	+0.0006	+1.27	+0.0006	+1.30
7 ^c	Primary	2,453,180.7529	-2.0	0.0010	+0.0068	+6.61	+0.0069	+6.89
8.....	Primary	2,453,183.7752	-1.0	0.0005	-0.0009	-1.66	-0.0008	-1.63
9.....	Primary	2,453,186.8061	+0.0	0.0003	-0.0001	-0.22	-0.0001	-0.16
10.....	Primary	2,453,189.8354	+1.0	0.0019	-0.0008	-0.44	-0.0008	-0.43
11.....	Primary	2,453,192.8694	+2.0	0.0015	+0.0031	+2.01	+0.0031	+2.03
12.....	Primary	2,453,247.4075	+20.0	0.0004	+0.0000	+0.05	+0.0001	+0.16
13.....	Secondary	2,453,309.5294	+40.5	0.0036	+0.0055	+1.53	-0.0005	-0.15

^a Forced $e = 0$.

^b Allowed e and ω to float.

^c This event was excluded from the fit (see text).

velocities, in addition to those reported by Alonso et al. (2004), we used the measurements by Laughlin et al. (2005), which are of higher internal precision and provide complementary phase coverage, particularly near the time of secondary eclipse.

We mapped the resulting χ^2 surface by performing orbital solutions for fixed values of e and ω over a densely sampled grid of these values. In each case we used the timings and radial velocities simultaneously, and we solved for the period and time of transit as well as the velocity semiamplitude and a velocity offset between the measurements by Laughlin et al. (2005) and those of Alonso et al. (2004). In Table 1, we list the observed minus calculated ($O - C$) times and relative errors $(O - C)/\sigma_{\text{HJD}}$, where σ_{HJD} represents the uncertainties in the timing measurements. We list these values both for the best-fit orbit for which we forced $e = 0$ and for the solution for which we allowed e and ω to vary (in which case the best-fit values were $e = 0.041$ and $\omega = 274^\circ.4$; see next paragraph). We present these times, as they will likely find a variety of additional applications, such as the search for additional planets (Agol et al. 2004; Holman & Murray 2005). We note that allowing e and ω to vary noticeably improved the fit to the time of secondary eclipse (see Table 1), reducing the value of $(O - C)/\sigma_{\text{HJD}}$ from +1.53 to -0.15.

A contour plot of the $\chi^2(e, \omega)$ surface and the corresponding limits on e and ω are shown in Figure 4. The minimum of this surface occurs at $e = 0.041$ and $\omega = 274^\circ.4$. The allowed $\{e, \omega\}$ parameter space is very small yet highly correlated. The eccentricity is consistent with zero; however, a value as large as $e = 0.06$ is permitted for a small range of values of $\cos \omega$ near 0. In particular, $e > 0.02$ requires $270^\circ < \omega < 285^\circ$, which would mean the orbital ellipse is nearly aligned with our line of sight. Additional radial velocity measurements at key portions of the orbital phase will serve to further restrict the allowed range of parameter space.

Bodenheimer et al. (2001, 2003) and Laughlin et al. (2005) have proposed that the tidal dissipation of a nonzero orbital eccentricity could generate an internal energy source sufficient to increase significantly the planetary radius. The precise value of the planetary radius could be used to infer the presence (or absence) of a rocky core, which would be a critical clue to the formation process of this planet. However, this effect is masked if an additional source of energy serves to preserve an inflated value for the planetary radius (Laughlin et al. 2005). Hence, it is important for us to evaluate the size of this energy term for

TrES-1, even if its radius is already roughly consistent with model expectations.

The circularization timescale τ_{circ} for TrES-1 is given by (Goldreich & Soter 1966)

$$\tau_{\text{circ}} = \frac{e}{\dot{e}} = \left(\frac{2PQ_p}{63\pi} \right) \left(\frac{M_p}{M_*} \right) \left(\frac{a}{R_p} \right)^5 \simeq 0.21 \left(\frac{Q_p}{10^6} \right) \text{ Gyr}, \quad (6)$$

where Q_p is the tidal quality factor. There is a large uncertainty in the likely value of Q_p . Terquem et al. (1998) find that Q is of the order of 10^6 for stars (based on the tidal circularization of main-sequence binaries), and Yoder & Peale (1981) constrain the value for Jupiter to the range $6 \times 10^4 < Q_{\text{Jup}} < 2 \times 10^6$ (based on the Jupiter-Io interaction). For an assumed value of Q_p , the timescale in equation (6) can then be used to estimate the rate of energy dissipation in the planet (Bodenheimer et al. 2003):

$$\dot{E}_d = \frac{e^2 GM_* M_p}{a \tau_{\text{circ}}} \simeq 4.3 \times 10^{28} e^2 \left(\frac{10^6}{Q_p} \right) \text{ ergs s}^{-1}. \quad (7)$$

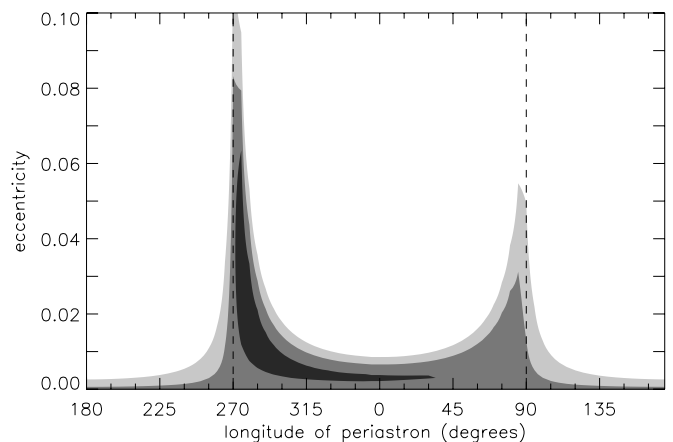


FIG. 4.—The 1 σ , 2 σ , and 3 σ confidence spaces of the orbital eccentricity e and the longitude of periastron ω . Since it is the combined expression $e \cos \omega$ that is constrained by the time of secondary eclipse, there exists a small range of ω (near $\cos \omega = 0$) for which a significant eccentricity is permitted. For this situation to occur, however, the orbital ellipse would need to be very nearly aligned with our line of sight. Additional radial velocity observations will further restrict the allowed parameter space.

If TrES-1 has no solid core, a value of $\dot{E}_d \lesssim 1 \times 10^{26}$ ergs s⁻¹ (Laughlin et al. 2005; also G. Laughlin 2005, private communication) is required; otherwise, the observed radius is too small. Using equation (7), we find that this, in turn, requires $e \lesssim 0.048(Q_p/10^6)^{1/2}$, which indeed appears consistent with our findings. We encourage additional radial velocity observations at key portions of the orbital phase. When combined with the times of primary and secondary eclipse presented in Table 1, such data will shrink the allowed range of values for the eccentricity and, by implication, further constrain the rate of energy dissipation.

This discussion serves to motivate similar work for HD 209458b. In contrast to TrES-1, its radius requires an internal source of energy. The detection of a significantly nonzero eccentricity for HD 209458b would provide strong support for this scenario. Of the various models for the inflated radius of a hot Jupiter (e.g., Bodenheimer et al. 2001; Guillot & Showman 2002; Burrows et al. 2003), the tidal dissipation of orbital eccentricity most naturally leads to a variety of observed planetary radii, since only some systems may contain additional planets that serve to pump the orbital eccentricity.

Shortly after we submitted this manuscript, we learned of a similar detection by Deming et al. 2005b, which presents *Spitzer* MIPS 24 μ m photometry spanning a time of secondary eclipse of the HD 209458 planetary system. Additional *Spitzer* observations of these and other extrasolar planets will enable the first comparative studies of the thermal emission from these elusive objects.

This work is based on observations made with the *Spitzer Space Telescope*, which is operated by the Jet Propulsion Laboratory, California Institute of Technology, under NASA contract 1407. G. T. acknowledges partial support for this work from NASA Origins grant NNG04LG89G. R. A. acknowledges financial support from grants AyA2001-1571 and ESP2001-4529-PE of the Spanish National Research plan. We are grateful to Robert Kurucz for providing the model of the stellar flux. We thank Joseph Hora and John Stauffer for illuminating IRAC discussions, and we thank Drake Deming, Scott Gaudi, Robert Noyes, Dimitar Sasselov, Sara Seager, and Joshua Winn for comments that improved the manuscript.

REFERENCES

- Agol, E., Steffen, J., Sari, R., & Clarkson, W. 2004, MNRAS, in press (astro-ph/0412032)
- Alonso, R., et al. 2004, ApJ, 613, L153
- Bakos, G., Noyes, R. W., Kovács, G., Stanek, K. Z., Sasselov, D. D., & Domsa, I. 2004, PASP, 116, 266
- Baraffe, I., Chabrier, G., Barman, T. S., Allard, F., & Hauschildt, P. H. 2003, A&A, 402, 701
- Barman, T. S., Hauschildt, P. H., & Allard, F. 2001, ApJ, 556, 885
- Bodenheimer, P., Laughlin, G., & Lin, D. N. C. 2003, ApJ, 592, 555
- Bodenheimer, P., Lin, D. N. C., & Marling, R. A. 2001, ApJ, 548, 466
- Bouchy, F., Pont, F., Santos, N. C., Melo, C., Mayor, M., Queloz, D., & Udry, S. 2004, A&A, 421, L13
- Brown, T. M., Charbonneau, D., Gilliland, R. L., Noyes, R. W., & Burrows, A. 2001, ApJ, 552, 699
- Burrows, A. 2005, Nature, 433, 261
- Burrows, A., Hubbard, W. B., Lunine, J. I., & Liebert, J. 2001, Rev. Mod. Phys., 73, 719
- Burrows, A., Sudarsky, D., & Hubbard, W. B. 2003, ApJ, 594, 545
- Chabrier, G., Barman, T., Baraffe, I., Allard, F., & Hauschildt, P. H. 2004, ApJ, 603, L53
- Charbonneau, D. 2003, ASP Conf. Ser. 294, Scientific Frontiers in Research on Extrasolar Planets, ed. D. Deming & S. Seager (San Francisco: ASP), 449
- Charbonneau, D., Brown, T. M., Latham, D. W., & Mayor, M. 2000, ApJ, 529, L45
- Charbonneau, D., Brown, T. M., Noyes, R. W., & Gilliland, R. L. 2002, ApJ, 568, 377
- Charbonneau, D., Noyes, R. W., Korzennik, S. G., Nisenson, P., Jha, S., Vogt, S. S., & Kibrick, R. I. 1999, ApJ, 522, L145
- Cho, J. Y.-K., Menou, K., Hansen, B. M. S., & Seager, S. 2003, ApJ, 587, L117
- Christian, D. J., et al. 2004, Proc. 13th Cool Stars Workshop, ed. F. Favata, submitted (astro-ph/0411019)
- Collier Cameron, A., Horne, K., Penny, A., & Leigh, C. 2002, MNRAS, 330, 187
- Cooper, C. S., & Showman, A. P. 2005, ApJL, submitted (astro-ph/0502476)
- Deming, D., Brown, T. M., Charbonneau, D., Harrington, J., & Richardson, L. J. 2005a, ApJ, 622, 1149
- Deming, D., Seager, S., Richardson, L. J., & Harrington, J. 2005b, Nature, 434, 740
- Dunham, E. W., Mandushev, G. I., Taylor, B. W., & Oetiker, B. 2004, PASP, 116, 1072
- Fazio, G. G., et al. 2004, ApJS, 154, 10
- Goldreich, P., & Soter, S. 1966, Icarus, 5, 375
- Guillot, T., & Showman, A. P. 2002, A&A, 385, 156
- Henry, G. W., Marcy, G. W., Butler, R. P., & Vogt, S. S. 2000, ApJ, 529, L41
- Holman, M. J., & Murray, N. W. 2005, Science, 307, 1288
- Kallrath, J., & Milone, E. F. 1999, Eclipsing Binary Stars: Modeling and Analysis (New York: Springer)
- Konacki, M., Torres, G., Jha, S., & Sasselov, D. D. 2003, Nature, 421, 507
- Konacki, M., Torres, G., Sasselov, D. D., & Jha, S. 2005, ApJ, 624, 372
- Kurucz, R. 1993, CD-ROM 13, ATLAS 9 Stellar Atmosphere Programs and 2 km/s Grid (Cambridge: SAO)
- Kurucz, R. L. 1992, IAU Symp. 149, The Stellar Populations of Galaxies, ed. B. Barbuy & A. Renzini (Dordrecht: Kluwer), 225
- Laughlin, G., Wolf, A., Vanmunster, T., Bodenheimer, P., Fischer, D., Marcy, G. W., Bulter, R. P., & Vogt, S. S. 2005, ApJ, 621, 1072
- Leigh, C., Collier Cameron, A., Udry, S., Donati, J., Horne, K., James, D., & Penny, A. 2003, MNRAS, 346, L16
- Marley, M. S., Gelino, C., Stephens, D., Lunine, J. I., & Freedman, R. 1999, ApJ, 513, 879
- Menou, K., Cho, J. Y.-K., Seager, S., & Hansen, B. M. S. 2003, ApJ, 587, L113
- Moutou, C., Pont, F., Bouchy, F., & Mayor, M. 2004, A&A, 424, L31
- O'Donovan, F. T., Charbonneau, D., & Kotredes, L. 2004, AIP Conf. Proc. 713, The Search for Other Worlds, ed. S. Holt & D. Deming (New York: AIP), 169
- Pepper, J., Gould, A., & Depoy, D. L. 2004, AIP Conf. Proc. 713, The Search for Other Worlds, ed. S. Holt & D. Deming (New York: AIP), 185
- Pont, F., Bouchy, F., Queloz, D., Santos, N. C., Melo, C., Mayor, M., & Udry, S. 2004, A&A, 426, L15
- Richardson, L. J., Deming, D., & Seager, S. 2003a, ApJ, 597, 581
- Richardson, L. J., Deming, D., Wiedemann, G., Goukenleue, C., Steyert, D., Harrington, J., & Esposito, L. W. 2003b, ApJ, 584, 1053
- Seager, S., Whitney, B. A., & Sasselov, D. D. 2000, ApJ, 540, 504
- Sozzetti, A., et al. 2004, ApJ, 616, L167
- Sudarsky, D., Burrows, A., & Hubeny, I. 2003, ApJ, 588, 1121
- Terquem, C., Papaloizou, J. C. B., Nelson, R. P., & Lin, D. N. C. 1998, ApJ, 502, 788
- Udalski, A., Pietrzynski, G., Szymanski, M., Kubiak, M., Zebun, K., Soszynski, I., Szewczyk, O., & Wyrzykowski, L. 2003, Acta Astron., 53, 133
- Udalski, A., Szewczyk, O., Zebun, K., Pietrzynski, G., Szymanski, M., Kubiak, M., Soszynski, I., & Wyrzykowski, L. 2002a, Acta Astron., 52, 317
- Udalski, A., Szymanski, M. K., Kubiak, M., Pietrzynski, G., Soszynski, I., Zebun, K., Szewczyk, O., & Wyrzykowski, L. 2004, Acta Astron., 54, 313
- Udalski, A., et al. 2002b, Acta Astron., 52, 1
- Vidal-Madjar, A., Lecavelier des Etangs, A., Désert, J.-M., Ballester, G. E., Ferlet, R., Hébrard, G., & Mayor, M. 2003, Nature, 422, 143
- Yoder, C. F., & Peale, S. J. 1981, Icarus, 47, 1